NASA
~~Controlled~~
~~Distribution~~
Technical
Paper
4000

1996

An Optimal Deconvolution Method for Reconstructing Pneumatically Distorted Near-Field Sonic Boom Pressure Measurements

Stephen A. Whitmore, Edward A. Haering, Jr.,
and L.J. Ehernberger
Dryden Flight Research Center
Edwards, California

National Aeronautics and
Space Administration

Office of Management

Scientific and Technical
Information Program

NASA
~~Controlled~~
~~Distribution~~
Technical
Paper
4000

June 1996

An Optimal Deconvolution Method for Reconstructing Pneumatically Distorted Near-Field Sonic Boom Pressure Measurements

Stephen A. Whitmore, Edward A. Haering, Jr.,
and L.J. Ehernberger

CONTENTS

ABSTRACT

In-flight measurements of the SR-71 near-field sonic boom were obtained by an F-16XL airplane at flightpath separation distances from 40 to 740 ft. Twenty-two signatures were obtained from Mach 1.60 to Mach 1.84 and altitudes from 47,600 to 49,150 ft. The shock wave signatures were measured by the total and static sensors on the F-16XL noseboom. These near-field signature measurements were distorted by pneumatic attenuation in the pitot-static system. The near-field pressure signatures were corrected by modeling the magnitude and phase of the pitot-static sensors and accounting for their effects using optimal deconvolution. Measurement system magnitude and phase characteristics were determined from ground-based step-response tests and extrapolated to flight conditions using analytical models. Deconvolution was implemented using Fourier transform methods. Comparisons of the shock wave signatures reconstructed from the total and static pressure data are presented. The good agreement achieved gives confidence of the quality of the reconstruction analysis. Although originally developed to reconstruct the sonic boom signatures from SR-71 sonic boom flight tests, the methods presented here generally apply to other types of highly attenuated or distorted pneumatic measurements.

INTRODUCTION

When an aircraft flies faster than the local sonic velocity, pressure discontinuities develop at the vehicle surface and propagate outward to form shock waves. These waves form in places where sharp changes in the vehicle geometry occur, such as at the nose, tail, canopy, wing and body junctions, and engine inlets. The flow-field region where shock waves exist for each geometric discontinuity extends an approximately 250-ft radius from the aircraft and is referred to here as the *near-field* region. With increasing distance from the aircraft, variations in the local speed of sound cause the various shocks induced by geometric changes to gradually coalesce into two major shock waves (refs. 1, 2). This coalescence gives rise to the characteristic N-wave profile which sweeps along the ground and produces the well-known sonic boom effect. The region where the shock waves have coalesced into a single bow shock and a single tail shock is referred to here as the *far-field* region. The region where coalescence has begun but is incomplete is referred to as the *mid-field* region. Figure 1 shows the three sonic boom regions for the SR-71 aircraft (Lockheed Aerospace, Burbank, California).

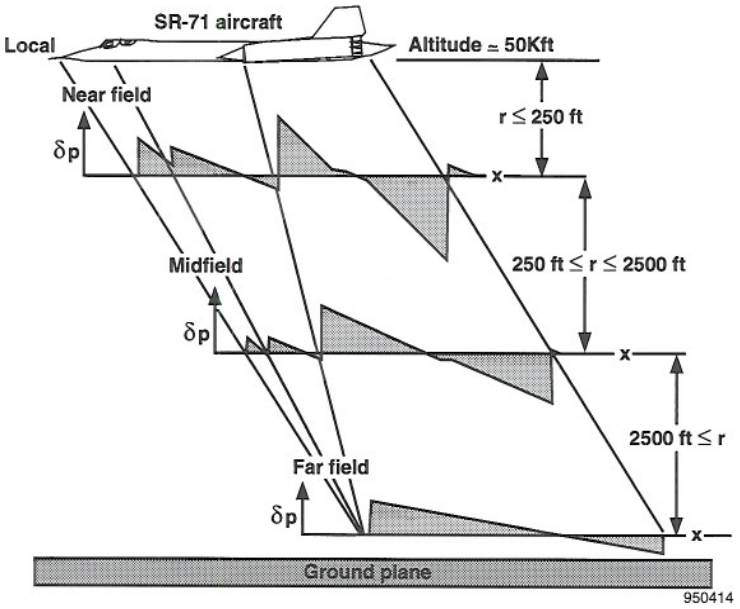

Figure 1. Near-, mid-, and far-field sonic boom signatures.

The perceived strength of a sonic boom is proportional to the peak overpressures which occur in the far-field region. Atmospheric factors which cause booms of significant strength to dissipate are not well understood. Analytical computations which describe the dissipative forces in the atmosphere were performed, but these computations are not well-supported by correlation with a broad base of experimental flight data (ref. 3). To benchmark the analytical code predictions, correlation of ground-based, far-field, sonic boom signature measurements with those measured in the near and midfields is necessary.

Data are relatively easy to obtain in the far-field, and a significant database exists for far-field measurements. To complete the picture, quality near-field sonic boom signatures are required. Unfortunately, because of the complexity of obtaining controlled measurements while operating in the near field of a supersonic aircraft, research quality signature measurements in the near field have never been satisfactorily obtained in-flight. To demonstrate the feasibility of making near-field measurements along the vertical centerline of a large supersonic aircraft at supersonic speeds, an experiment was conducted at NASA Dryden Flight Research Center (DFRC), Edwards, California (ref. 4). A probe aircraft was used to sense the near-field shock wave signature of an SR-71 aircraft. For these tests, an F-16XL aircraft (General Dynamics, Fort Worth, Texas) was used as the probe aircraft. The F-16XL aircraft was chosen because of its high Mach number flight envelope and its supersonic endurance. Shock wave signatures were measured by the F-16XL noseboom pitot-static system.

Conceptually, pitot-static pressure time histories can be correlated with vehicle trajectory data to infer the spatial distribution of the near-field signature. In practice, however, the task is not as straight forward. Raw measurements resulting from the F-16XL pitot-static system were badly distorted. These pressure distortions were primarily caused by pneumatic attenuation in the airdata measurement system. In addition, the local flow-field of the F-16XL aircraft affected the raw pressure data.

This paper describes a novel method for reconstructing the sonic boom signature by modeling the magnitude and phase characteristics of the pitot-static systems and accounting for their effects using optimal deconvolution. Pressure sensor magnitude and phase were determined from ground-based step-response tests and extrapolated to flight conditions using analytical models. To remove the F-16XL local flow-field effects, reference total and static pressure time histories were computed. These reference time histories represent the total and static pressure fields which would occur in the absence of the SR-71 aircraft. The reference time histories were constructed from data sources independent of the F-16XL pitot-static measurement system. To evaluate the shock wave signatures, the reference pressure time histories were subtracted from the deconvolved pressure time histories. Examples of reconstructed flight signatures are presented in the Flight Test Procedures, Analysis, and Results section.

BACKGROUND

Mullens (ref. 5), Smith (ref. 6), and Maglieri (ref. 7) have obtained in-flight signature measurements. Mullens' data were obtained from 85 to 1770 ft below and from 100 to 1420 ft to the side of an F-100 airplane at Mach 1.05.

A General Dynamics (Fort Worth, Texas) B-58 bomber airplane served as the boom generator during the Smith and Maglieri investigations. Smith's results include data for the F-100 and F-104 airplanes at Mach 1.2 and data for the B-58 from Mach 1.3 to Mach 1.8. Data were obtained for lateral separation distances from 120 to 425 ft. The investigation was conducted to determine the near-field-flow patterns for assessing the dangers of close-formation flying.

Maglieri's data were obtained at distances from 1300 to 9100 ft below and from 1700 to 2000 ft above the B-58 aircraft from Mach 1.42 to Mach 1.69. Emphasis was on obtaining data to assess the lift and volume interaction effects on the near-field signatures of a delta-wing bomber. For the experiments conducted in refs. 5–7, the data are either too low in Mach number, not below the generating aircraft, or too far away for the present needs of bench-marking analytical computations. These results are summarized in table 1.

Table 1. Previous sonic boom signature measurement flight tests (refs. 5 – 7).

Investigator	Aircraft	Mach number	Distance and position	
Mullens, 1956	F-100	1.05	85 – 1770 ft below	100 – 1420 ft to side
Smith, 1960	B-58, F-100, F-104	1.2 – 1.8	120 – 425 ft to side	
Maglieri, 1963	B-58	1.42 – 1.69	1300 – 9100 ft below	1700 – 2000 ft above

VEHICLE AND INSTRUMENTATION DESCRIPTIONS

As mentioned in the Introduction section, the SR-71 airplane was chosen as the shock-generating vehicle, and the F-16XL airplane was chosen as the probe aircraft. This section describes these vehicles and discusses the instrumentation systems available on each vehicle.

SR-71 Aircraft

Figure 2 shows the SR-71 aircraft. This aircraft is one of three at DFRC that is on loan from the U. S. Air Force. This two-place, delta-wing aircraft was formerly used for military reconnaissance. Powered by two J-58 axial-flow turbojets (Pratt & Whitney, West Palm Beach, Florida), an SR-71 aircraft can sustain a cruise of Mach 3.2 at an altitude of 85,000 ft (ref. 8). The vehicle instrumentation used in this analysis includes the inertial navigation system (INS), astro-navigation system (ANS), and airdata measurements. These airdata measurements are teed off from the production airdata probe to NASA-supplied transducers. Data from these sensors were intercepted from the ship communication bus by a pulse code modulation (PCM) system interface and telemetered to ground for real-time monitoring and postflight analysis. Flight trajectory was monitored and recorded by ground-based, C-band radar. The radar data stream was merged with the aircraft telemetry data stream postflight for research analysis.

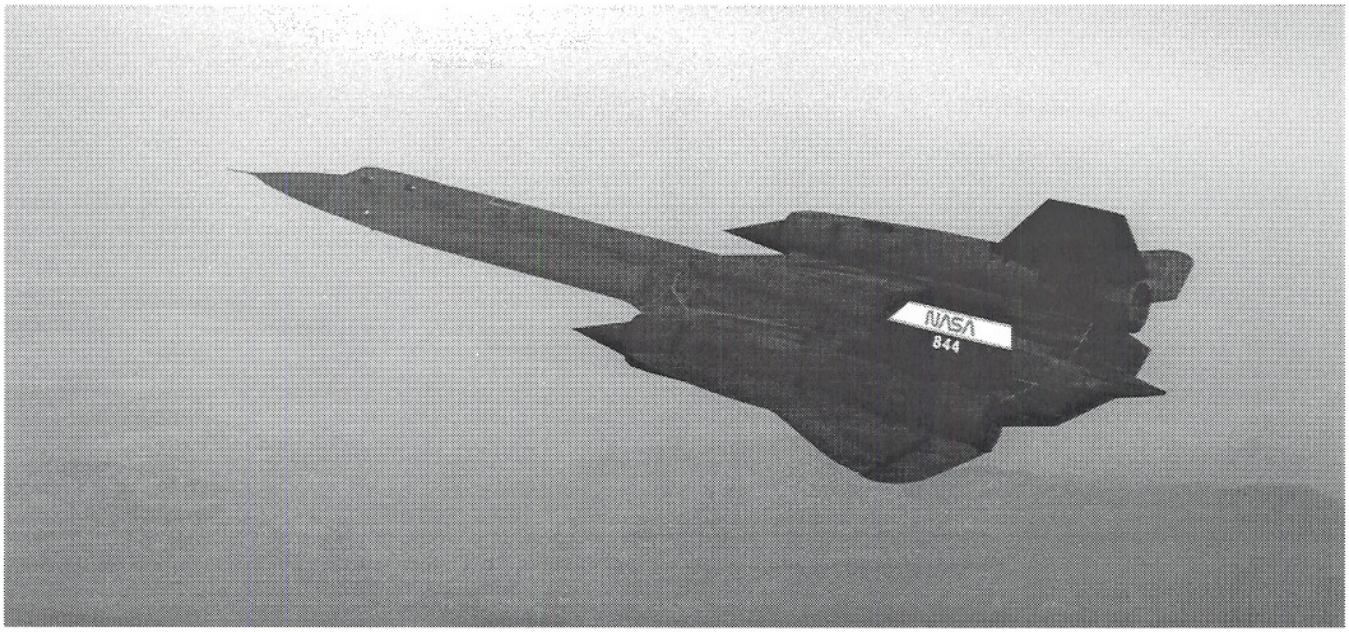

EC 92 09241-1

Figure 2. The SR-71 aircraft.

F-16XL Aircraft

Figure 3 shows the F-16XL airplane. This airplane is powered by a nonproduction F110-GE-100 turbofan engine (General Electric, Lynn, Massachusetts) (ref. 9). The F-16XL aircraft has been flight tested to a maximum of Mach 2.05 and a peak altitude of 65,000 ft. The vehicle is outfitted with a research-quality instrumentation system with airdata being obtained with a nose-boom-mounted pitot-static airdata probe. Total pressure measurements were provided by a single pitot port at the boom tip, and static measurements were provided by a partial ring of static pressure ports located circumferentially on the boom. For this analysis, total and static pressure were teed off from the noseboom pressure supply lines and were sensed by a set of identical absolute digital pressure transducers whose full-scale ranges were 0 – 2736 psf (0 – 19 psi) with a digital resolution of 18 bits (0.01 psf). The total and static pressure transducers had measured 3 standard deviation, σ, accuracies of approximately ± 0.0075 percent of the calibrated full-scale (± 0.21 psf). In addition to the research instrumentation, the total and static pressure inputs supplied the ship's system central airdata (CAD) computer and the cockpit instrumentation gauges. This additional instrumentation added considerably to the volume entrapped within the sensing systems and contributed largely to the measurement magnitude and phase distortions described in the Ground Test Procedures, Analysis, and Results section. The total volume entrapped in the static-pressure-measuring system was roughly four times that of the total pressure system.

Other research measurements included inertial navigation parameters from the INS and space positioning and velocity data from a ground-based radar track of the C-band beacon. The radar data stream was merged with the aircraft telemetry data stream postflight for research analysis. Onboard data measurements were collected by the 10-bit PCM system, recorded onboard with an analog tape recorder, and telemetered to ground in encoded form. The 18-bit, airdata pressure measurements were collected as two 10-bit words. These words were concatenated on the ground during postflight data analysis.

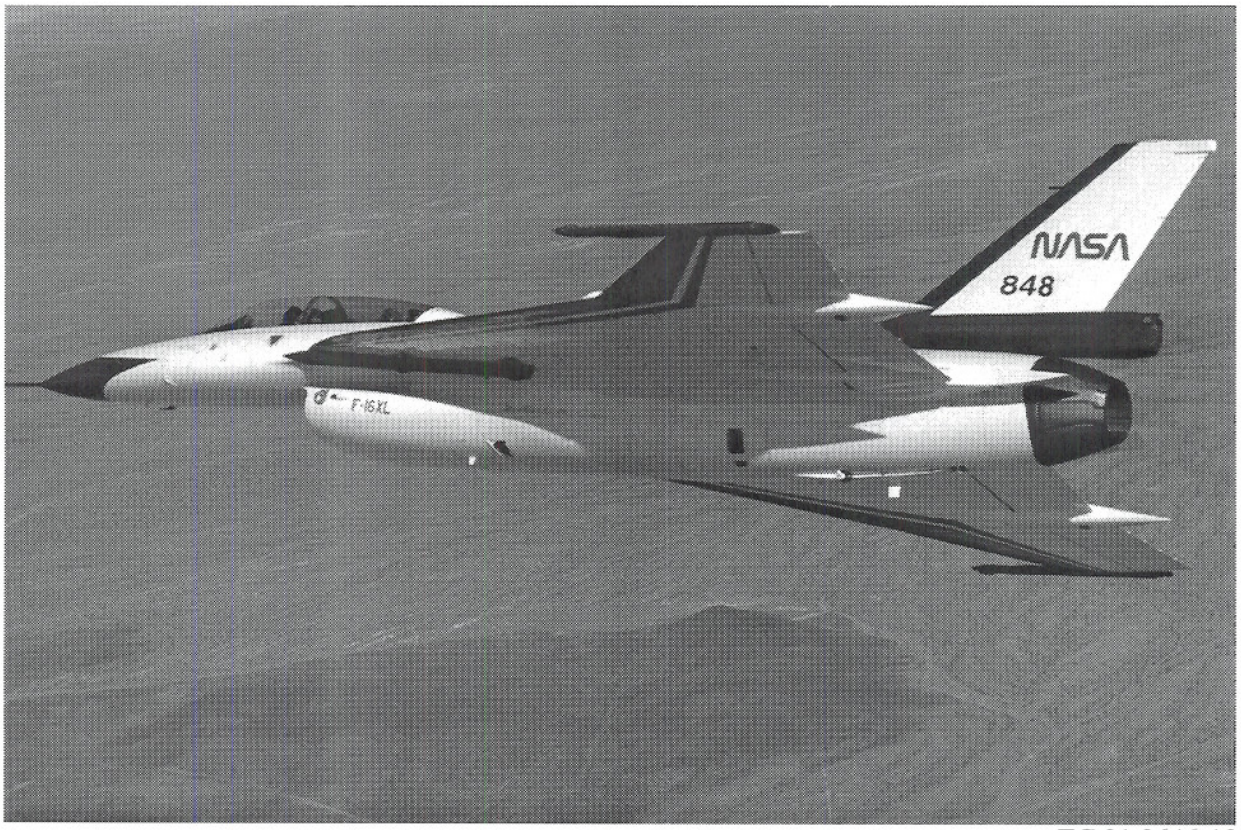

EC 91 0646-10

Figure 3. The F-16XL aircraft.

RESULTS AND DISCUSSION

This section summarizes the results of ground-based, step-response tests used to determine the pressure sensor magnitude and phase characteristics, flight test maneuvers used to obtain the raw pressure data, and analysis used to reconstruct the sonic boom signatures. Results from the flight tests, including representative boom signature data, are presented.

Ground Test Procedures, Analysis, and Results

This subsection describes the ground test procedures used to estimate the airdata system parameters. Analysis methods are described, and results of the ground tests are presented.

Procedures

Because spatial distribution of the near-field, sonic boom signature must be inferred from the time correlation of pressure and space positioning data, the magnitude and phase characteristics inherent to the F-16XL pitot-static system must be well-known. Unfortunately, the internal pneumatic layout of the CAD computer and the cockpit displays is unknown, and accurately modeling the responses of the system components analytically is impossible. To determine the baseline response characteristics of the measurement system, a series of simple, ground-based, step-response tests was performed.

The step-response test procedures are described next. First, a pressure fitting was attached to the total pressure portion of the noseboom. Then, a "Y" connector was attached to this fitting. One branch of the "Y" was connected to an accurate reference pressure calibration unit. The other branch of the "Y" had a short length of tubing called the vent line. The vent line was doubled over on itself and held sealed with a surgical hemostat. Next, the total pressure side of the airdata system was then evacuated or pressurized to the desired level above or below the ambient pressure. When the pressure stabilized, the tubing between the calibration unit and the noseboom was doubled over and sealed with a second hemostat as close as possible to the noseboom. To vent the system to ambient pressure condition, the first hemostat on the vent line was rapidly opened allowing a sharp pressure change to be introduced to the total pressure system. After the system reached ambient pressure level, the vent line was resealed using the hemostat and pressurized (or evacuated) to the next test condition. Lastly, after the total pressure tests were completed, step-response tests on the static pressure system were conducted using an identical procedure.

To evaluate the range of pressure rises, ground tests were performed for positive and negative step inputs with data being acquired for steps with ± 0.1, ± 0.5, and ± 1.0 psi magnitudes. These data responses were recorded using the F-16XL onboard data acquisition system at a rate of 25 samples/sec. Ambient conditions were recorded off-line using a hand-held barometer and thermometer. These data were used later in the posttest analysis. For each condition, the step-response tests were repeated twice.

Analysis

For small step inputs, laminar flow conditions exist in the pneumatic system. The analysis presented in appendix A demonstrates that total and static airdata system responses can be closely approximated by a second-order system. The transducer measurements are the system output, and external pressure provides the system input. Appendix A also presents a method to extrapolate the ground test natural frequencies and damping ratios to flight conditions. Appendix B describes the parameter identification method used to extract the system parameters from the ground tests.

Results

The results of the step-response tests were averaged for the total and static pressure systems. Table 2 lists the averaged natural frequencies, damping ratios, and time lags.

Selected comparisons of the second-order response fits to the measured data are presented in figures 4(a) and 4(b) for the total pressure system and in figures 5(a) and 5(b) for the static pressure system. Clearly, the second-order model provides a good fit to the ground-based data.

Table 2. Ground test results for the second-order system parameters.

Pressure system	Natural radian frequency, rad/sec (Hz)	Damping ratio	Time lag, sec
Total	17.47 (2,780)	0.841	0.096
Static	8.485 (1.351)	2.254	0.531

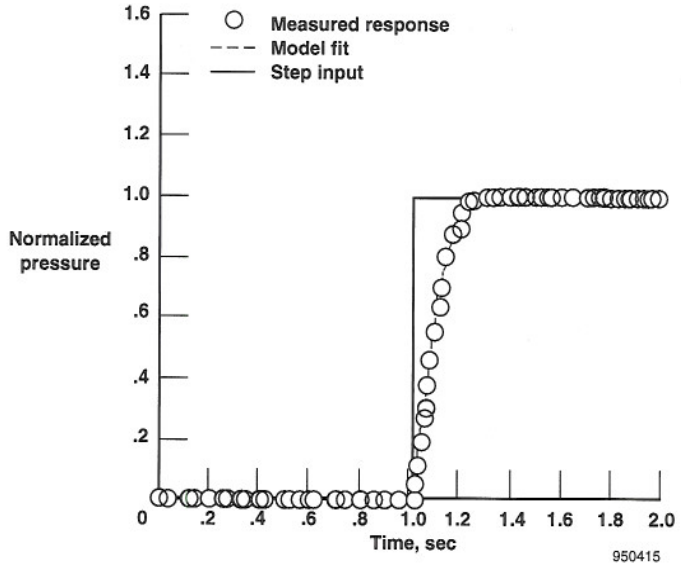

(a) $\delta p = 0.480$ psi.

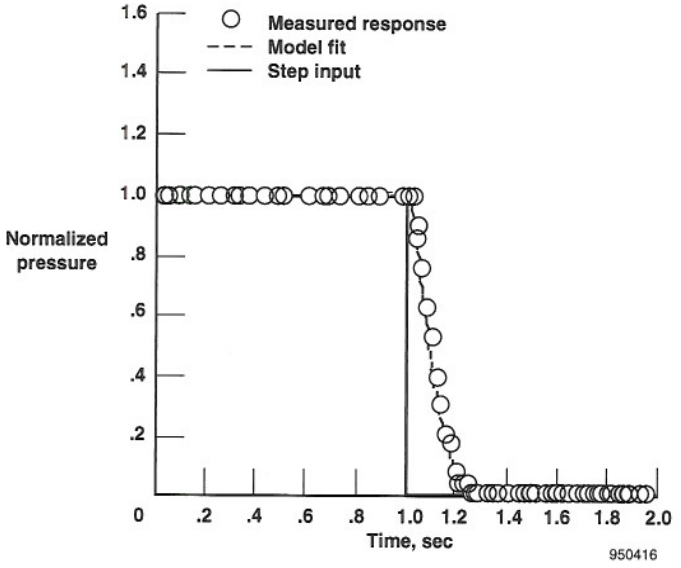

(b) $\delta p = -0.493$ psi.

Figure 4. Normalized step-response tests: Comparisons of model fits with data for total pressure system.

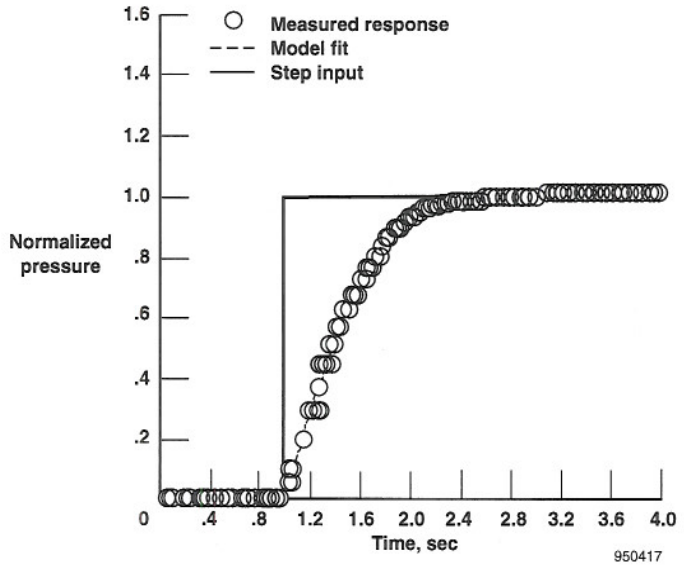

(a) $\delta p = 0.488$ psi.

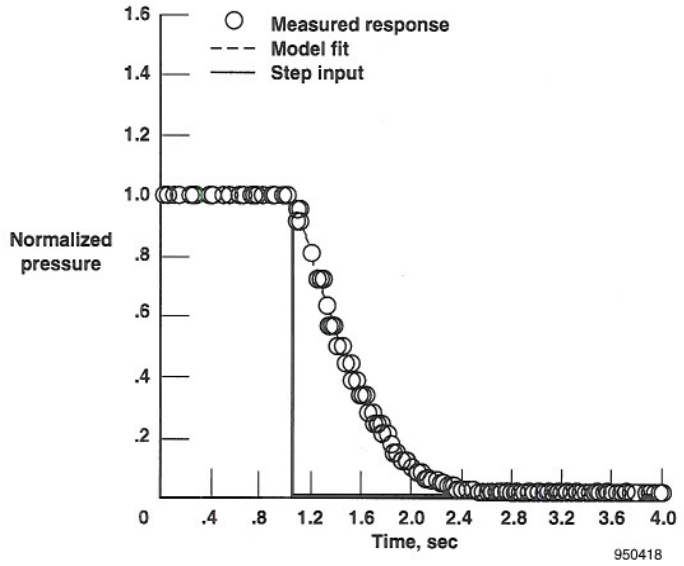

(b) $\delta p = -0.495$ psi.

Figure 5. Normalized step-response tests: Comparisons of model fits with data for static pressure.

Flight Test Procedures, Analysis, and Results

This subsection describes the flight test procedures used to gather the raw sonic boom data. Methods used to reconstruct the sonic boom signatures are described, and results of the analysis are presented. Comparisons of boom signatures reconstructed using static and total pressure data are presented.

Procedures

The F-16XL aircraft was positioned on the vertical plane of symmetry behind and below the SR-71 aircraft at the required vertical separation distance. As the F-16XL aircraft probed forward into the shock field of the SR-71 aircraft, the pilot could see when the F-16XL passed through the shock waves. The F-16XL pilot described this shock as looking

"like a sheet of water." The encounter times were marked for later correlation with telemetered data. In all, 22 signatures were obtained from Mach 1.60 to Mach 1.84 and at altitudes from 47,600 to 49,150 ft. Flightpath separation distances between the vehicles varied from 40 to 740 ft.

The desired overpressure signature is the difference between the corrected pressures sensed at the noseboom and a reference pressure. Reference pressure represents the pressure that would have occurred in the absence of the SR-71 aircraft. As the F-16XL aircraft probed the SR-71 shock field, interactions with SR-71 shock waves made it impossible for the probe aircraft to maintain a steady separation and velocity through the flow field. These speed and altitude variations significantly affected the pressure values sensed at the noseboom. Thus, the reference pressure data must be reconstructed using trajectory data that are measured independently from the F-16XL noseboom. This reconstruction is discussed in the Analysis subsection.

This procedure was used to reconstruct the respective sonic boom signatures. Results of the ground-based, step-response tests were extrapolated to flight conditions using the method described in appendix A. The raw pitot-static pressure measurements were corrected for the effects of pneumatic distortion using the method described in appendix C. Next, the reference pressure time histories were generated and subtracted from the deconvolved signatures to give the shock wave overpressure measurement. For this analysis, signatures from the static and total pressure measurements were analyzed separately.

Analysis

Data sources used to generate the reference pressure data were radar space positioning and velocities (ref. 10), INS attitudes and velocities, and weather parameters. These weather parameters included windspeed and direction, ambient pressure, and ambient temperature from meteorological analysis or rawindsonde weather balloon data and National Weather Service charts (ref. 11). The static pressure measured by the static pressure sensor before penetration of the SR-71 shock wave field was used as the baseline zero overpressure. As the F-16XL aircraft probed the shock field of the SR-71 aircraft, the reference static pressure data were generated using variations in radar-derived altitude and the hydrostatic equation (ref. 12). To give variations in the total pressure baseline, a reference airspeed was computed from inertially derived ground speed data (either radar or INS), and windspeeds were computed from the meteorological analysis. Temperature from the meteorological analysis was used to compute the reference Mach number from the reference airspeed data. Using the Rayleigh pitot equation (ref. 14), the reference total pressure data were generated using the reference Mach number and static pressure data.

Results

Sample sonic boom time history signatures are presented next. These data are representative of all results obtained during the sonic boom flight tests. Comparisons of the raw and deconvolved pressure signatures is presented first. Next, the reference pressure data are subtracted to yield sonic boom overpressure time histories. Lastly, signatures obtained using total and static pressure data are evaluated independently, and the results are compared.

Figure 6 illustrates the effect of the deconvolution on the raw signature measurements. These data were obtained in the near field at a vertical separation distance of 200 to 260 ft below the centerline of the SR-71 aircraft. Here, the shock wave field was probed from the rear of the SR-71 aircraft moving forward. Time histories of raw and deconvolved static and total pressure are shown. Shock waves generated by the aircraft tail, inlet, canopy, and bow are labeled. Raw total pressure is slightly lagged from the deconvolved data and has a slightly higher amplitude. In this case, the total pressure sensor is mildly resonant, and the deconvolution algorithm acts as a signal attenuator. On the other hand, when compared to the deconvolved static pressure data, the raw static pressure has been greatly lagged and attenuated. The raw static pressure is more heavily attenuated than the total pressure measurement because the system pressure level is considerably lower. In addition, the entrapped volume in the static pressure system is larger by a factor of approximately four. See appendix A.

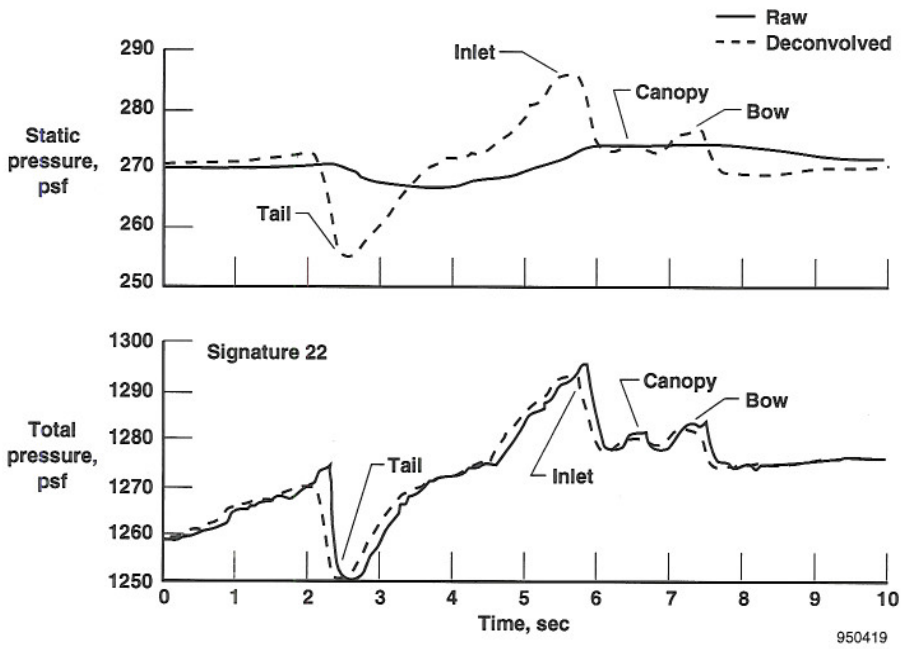

Figure 6. Comparisons of raw and deconvolved shock wave pressure signatures (200 – 260 ft below vertical separation).

The reference pressure data represent the pressures that would be sensed in the absence of the SR-71 aircraft. Using the data of figure 6, comparisons of the deconvolved pressure data and the reference data for the static and total pressures are presented in figures 7(a) and 7(b). Note that little variation exists in the reference static pressure. Because of probe aircraft speed and separation variations as the F-16XL aircraft penetrated the SR-71 shock field, large variations occurred in reference total pressure during the maneuver.

Using the data of figures 6 and 7, comparisons of signatures derived from the deconvolved static and total pressure data are presented in figure 8. Raw signatures reconstructed by subtracting the reference pressures from the undeconvolved pressure measurements are also presented. Clearly, the raw signatures are radically different for the total and static pressures. On the other hand, the deconvolved total and static pressure signatures show close agreement.

Note that the static and total pressure signatures were obtained from fundamentally different flow-field measurements. In addition, at high Mach numbers, shock wave losses cause the overpressures measured by the two types of sensors to disagree. However, for these test conditions, simple adiabatic analysis (ref. 13) showed that in the absence of other measurement errors overpressures measured by the static and total pressure measurements should closely agree. Because these total and static pressure signatures were derived independently, the good agreement between the signatures gives confidence in the validity of the deconvolution and trajectory analysis. Although deconvolution analysis gives a good representation of overpressure time histories, because of jostling of the probe aircraft as it penetrated the SR-71 shock field, these data were not obtained at a constant separation distance.

Figure 9 shows similar comparisons for the midfield (580 – 740 ft below). For these data, the field was measured from front to aft as the probe aircraft decelerated. Thus, the signature appears to be backward when compared to figure 8. Notice in figure 9 that there is no distinct canopy shock. At this large separation distance (580 – 740 ft), the canopy shock has been absorbed by the inlet shock. This absorption is a normal feature of the shock coalescence process.

Finally, signatures measured in the very near field (40 – 90 ft below) are presented in figure 10. For this maneuver, the field probe was performed below and to the side of the SR-71 aircraft. This causes the engine inlet shocks to appear as two distinct shocks. For the near-field data of figure 10, the very large tail shock strength is underpredicted by the static pressure data. On the other hand, for the signatures measured in the mid- and far-fields, the static and total pressure data give approximately the same tail shock strengths. Analysis presented in appendix D suggests that this discrepancy results from turbulent flow conditions being induced in the static pressure system by large pressure gradients. When turbulent flow is induced in the static pressure system, the tube damping rises dramatically. In addition, the second-order deconvolution model, which uses laminar flow assumptions, underpredicts the size of the shock wave.

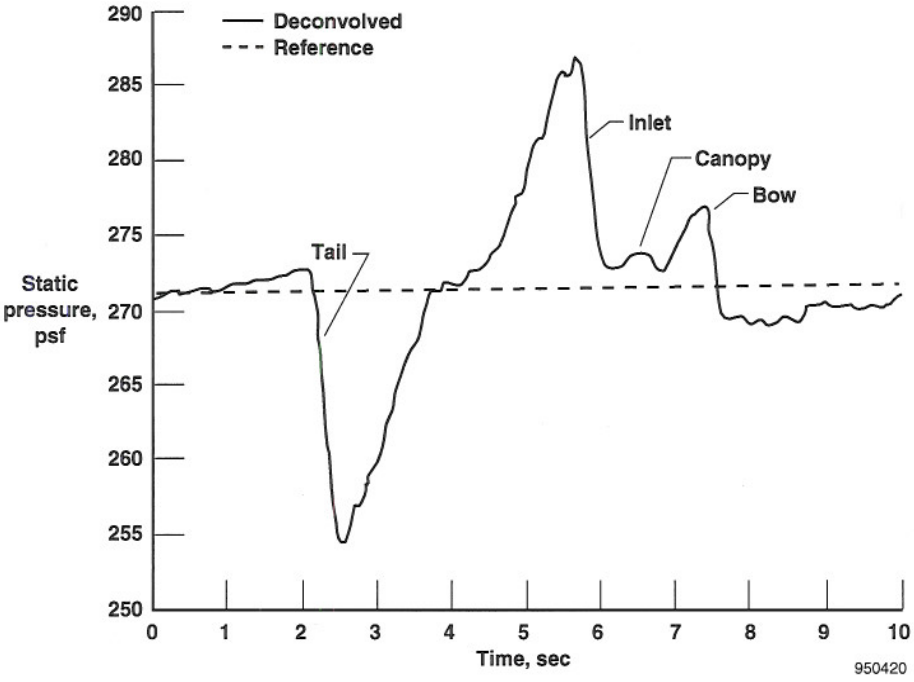

(a) Static pressure.

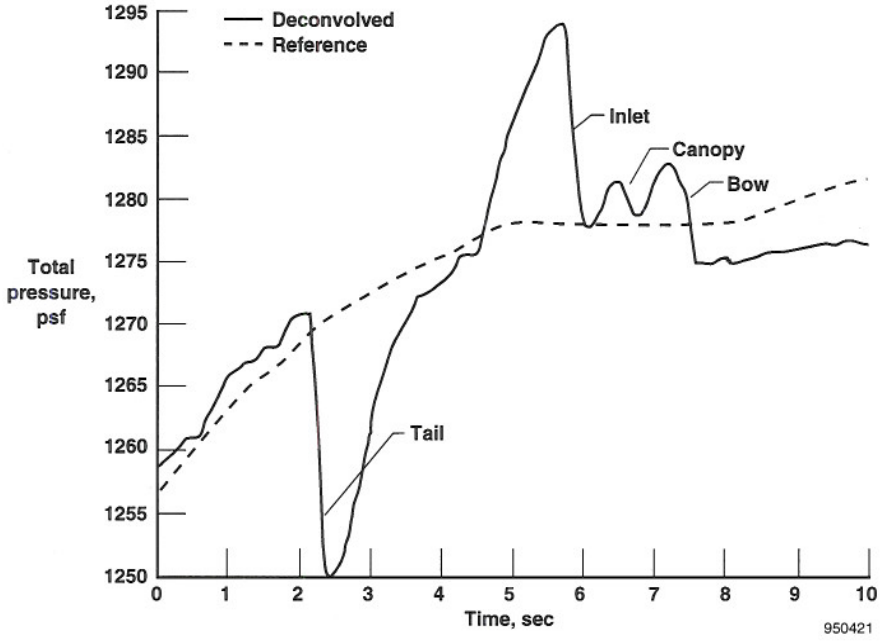

(b) Total pressure.

Figure 7. Comparisons of deconvolved and reference pressure data (200 – 260 ft below vertical separation distance).

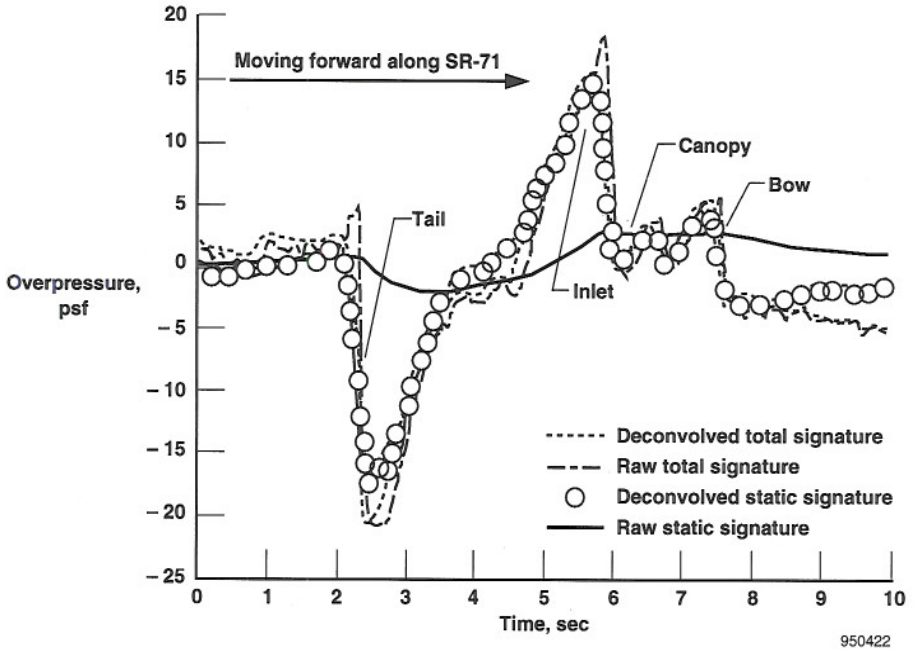

Figure 8. Comparisons of static and total pressure derived sonic boom signatures (200 – 260 ft below vertical separation distance).

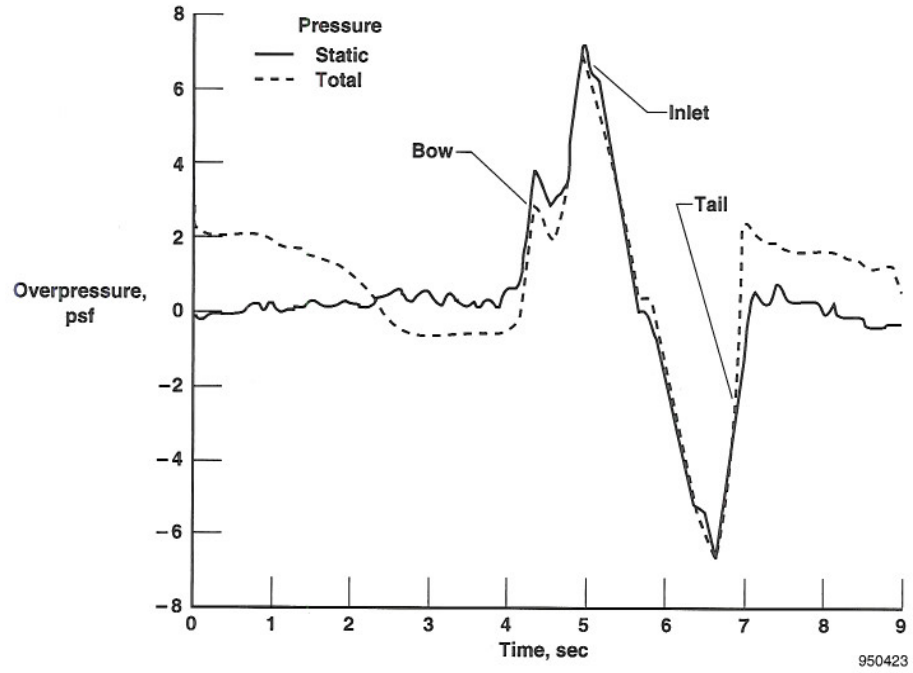

Figure 9. Midfield shock overpressure signature comparisons (580 – 740 ft below vertical separation distance). Note that the field was probed from front to back.

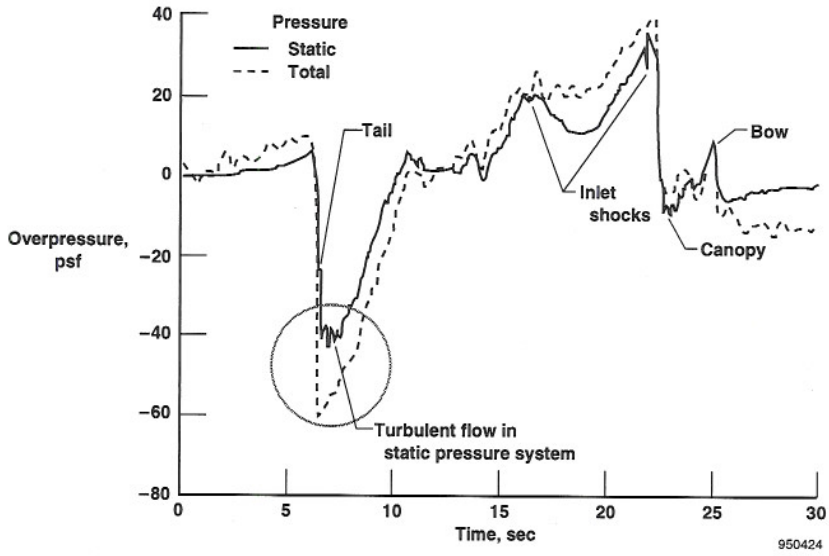

Figure 10. Comparisons of sonic boom signatures for very near field (40 – 90 ft below vertical separation distance).

Figure 11 presents the approximate boundaries for the maximum allowable difference between the external and measured pressures (P_0 and P_L) which can be tolerated without inducing transitional flow within the tube. Here, the shaded regions will have maximum Reynolds numbers which are less than the tube flow transition Reynolds number of 2300. Total pressure can have higher step inputs with increasing Mach number without inducing transitional flow. At the flight conditions of figures 6 through 9, the total pressure system (fig. 11(a)) can sustain a maximum pressure difference in the tube of nearly 50 psf without going turbulent. The static pressure system (fig. 11(b)) can sustain a maximum difference of approximately 40 to 45 psf without becoming turbulent.

For the near-field signature data, turbulent flow is induced in the static pressure system by the tail shock because the system response latency allows a large pressure gradient to form. This pressure gradient induces sizable tube flow velocities, and the critical transition Reynolds number is exceeded (ref. 18). Turbulent flow does not form in the total pressure-measuring system because the system response equalizes the pressure within the tube before large flow velocities can build up. For the very near-field data of figure 10, the differences between the deconvolved total pressure signature and raw total and static pressure signatures are plotted in figure 12. Clearly, the pressure differential level for the total pressure system is well below the level required to reach critical Reynolds number. On the other hand, at the tail shock, the static pressure differential exceeds the critical threshold.

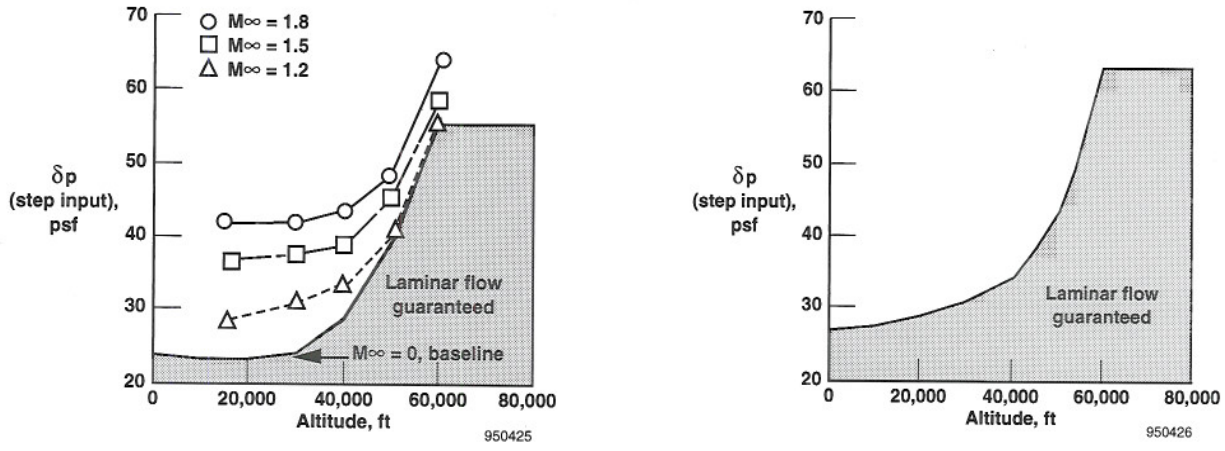

(a) Total pressure system.

(b) Static pressure system.

Figure 11. Maximum allowable pressure differential in systems for laminar flow.

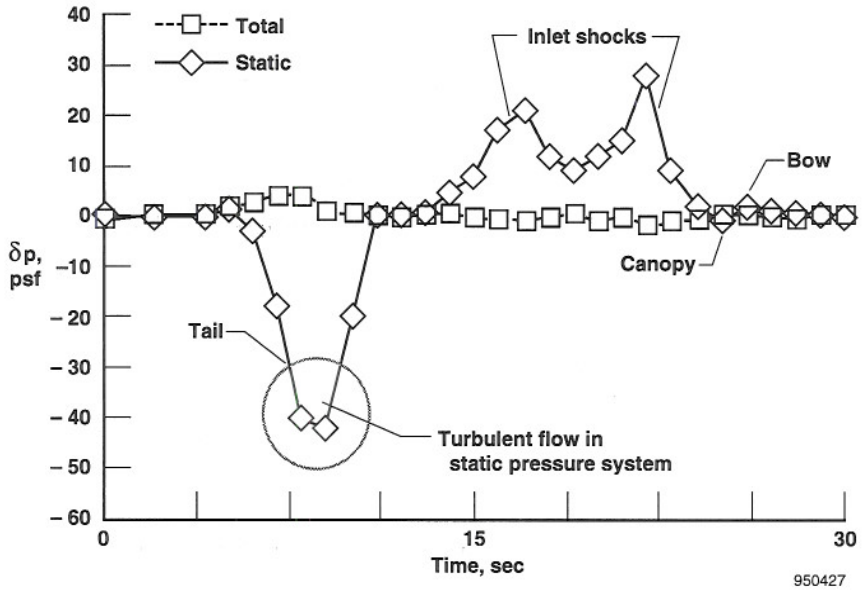

Figure 12. Maximum internal pressure differential for very near-field total and static pressure measurement systems (40 to 90 ft below vertical separation distance).

CONCLUDING REMARKS

In-flight measurements of the near-field SR-71 shock wave pressure field were obtained at separation distances ranging from 40 to 740 ft by probing with the noseboom pitot-static system of an F-16XL airplane. The raw pitot-static measurements were distorted by pneumatic distortion and influences of the probe aircraft flow field. This paper develops a novel method to correct for these distortions.

Pneumatic distortions were corrected by modeling the pneumatically induced magnitude and phase distortions and by accounting for their effects using optimal deconvolution. The local flow-field effects were removed by construction reference time histories of the total and static pressure which would occur in the absence of the SR-71 shock waves and subtracting the results from the deconvolved pressure data. The pitot-static measurement system magnitude and phase characteristics were determined from ground-based step-response tests and extrapolated to flight conditions using analytical models. The deconvolution is implemented using Fourier transform methods. Reference time histories for total and static pressure were constructed using data sources independent from the pitot-static measurement system, including C-band radar tracking, inertial navigation system attitudes and velocities, and rawindsonde weather balloon sounding data.

Twenty-two signatures were obtained from Mach 1.60 to Mach 1.84 and altitudes from 47,600 to 49,150 ft. Examples of reconstructed flight signatures were presented. Agreements of signature shape and overpressure magnitude for the static and total pressure-derived signatures are excellent. This agreement gives confidence of the quality of the reconstruction analysis.

Although developed to reconstruct the sonic boom signatures from the SR-71 sonic boom flight tests, the methods described here apply to other types of highly attenuated or distorted pneumatic measurements. Other applications might include the reconstruction of pressure transients in piping systems from single point measurements and fidelity enhancement of unsteady pressure measurements.

Dryden Flight Research Center
National Aeronautics and Space Administration
Edwards, California, April 5, 1995

APPENDIX A

PITOT-STATIC SYSTEM RESPONSE MODEL

This appendix presents the pneumatic system model and reduces the model to a quasi-second-order system. Rules for extrapolating the system parameters to various flight conditions are developed for laminar flow conditions.

System Model

For simple tubing geometry (fig. A-1), the frequency response characteristics of the system may be expressed in closed form as (ref. 14)

$$\frac{P_L(s)}{P_0(s)} = \frac{1}{\cosh\left[\sqrt{\alpha}L/c\right] + \frac{V\sqrt{\alpha}}{A_c c}\sinh\left[\sqrt{\alpha}L/c\right]} \tag{A-1}$$

where α is the square of the damped radian frequency

$$\alpha = s^2 + \frac{R_a}{\bar{\rho}}\, s = -\omega^2 + j\,\frac{R_a}{\bar{\rho}}\,\omega \Rightarrow s \equiv j\omega \tag{A-2}$$

where

P_L	=	measured pressure
P_0	=	input pressure
$s = j\omega$	=	radian frequency
L	=	tube length
c	=	local speed of sound
D	=	tube diameter

where R_a is the acoustical impedance of the system, and $A_c = \pi D^2/4$ is the cross-sectional area of the tubing.

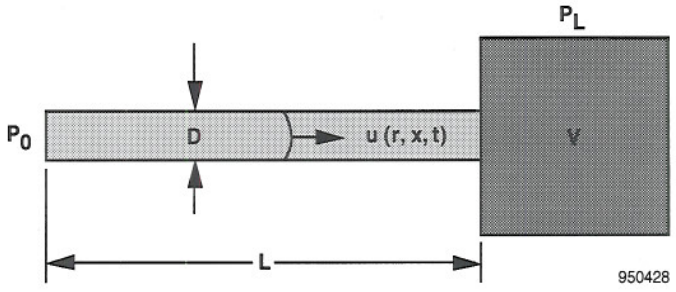

Figure A-1. Simple tubing geometry.

The acoustical impedance of the system is the resistance to flow with the tube and is proportional to the surface skin friction coefficient and the Reynolds number (refs. 15, 16),

$$R_a = \frac{2\mu R_{ey} C_f}{D^2} \tag{A-3}$$

where

C_f = skin friction coefficient

R_{ey} = Reynolds number

μ = dynamic viscosity

For one-dimensional tube flow with fully developed laminar flow conditions,

$$C_f = \frac{16}{R_{ey}} \tag{A-4}$$

Thus,

$$R_a = \frac{32\mu}{D^2} \tag{A-5}$$

System Model Reduction

For complex plumbing geometries in which branches or cascades occur, the basic solution, equation A-1, may be used as a building block to develop end-to-end solutions by modifying the boundary condition to allow recursive implementation. The frequency response at each node is given as a function of the frequency response of the previous node. This method, however, requires accurate knowledge of the system configuration. Unfortunately, the F-16XL airdata system has a complex plumbing arrangement with multiple lines, tees, compression fittings, trapped volumes, and transducer connections. As a result, knowing the precise geometric configuration of the system is difficult. Thus, analytical computations based on geometry assumptions would be highly suspect. Instead, it is assumed that for the sonic boom data set, the F-16XL systems can be represented by equivalent "single node" systems in which the damping and frequency are determined from ground experiments and extrapolated to flight conditions. Here, the geometry effects are determined using the ground-based, step-response data, and the results are extrapolated to flight conditions using physical rules.

To perform the analysis, first, the form of the analytical model must be reduced to a manageable form, so extrapolation rules can be developed. This model reduction is done by performing a Taylor series expansion of equation A-1, where

$$\cosh\left[\frac{\sqrt{\alpha}L}{c}\right] = \sum_{m=0}^{\infty} \left\{ \frac{\left[\frac{L}{c}\right]^{2m} \alpha^m}{(2m)!} \right\} \tag{A-6}$$

and

$$\sinh\left[\frac{\sqrt{\alpha}L}{c}\right] = \sum_{m=0}^{\infty}\left\{\frac{\left[\frac{L}{c}\right]^{2m+1}\alpha^{(2m+1)/2}}{(2m+1)!}\right\} \tag{A-7}$$

Substituting into equation A-1 and collecting like powers of α

$$\frac{P_L(s)}{P_0(s)} = \frac{1}{1+\sum_{m=1}^{\infty}\left[\left\{\frac{\left[\frac{L}{c}\right]^{2m}}{(2m)!}\right\}+\frac{V}{A_c c}\left\{\frac{\left[\frac{L}{c}\right]^{2m-1}}{(2m-1)!}\right\}\right]\alpha^m} \tag{A-8}$$

Evaluating equation A-2 where $\bar{\rho}$ is the longitudinal average of the tubing density and regrouping terms

$$\frac{P_L(s)}{P_0(s)} = \frac{1}{1+\left(\frac{L^2}{2c^2}+\frac{LV}{A_c c^2}\right)\left(s^2+\frac{R_a}{\bar{\rho}}s\right)+\left(\frac{L^4}{24c^4}+\frac{L^3 V}{6A_c c^4}\right)\left(s^2+\frac{R_a}{\bar{\rho}}s\right)^2+\ldots} \tag{A-9}$$

If all terms (in s) of equation A-9 of order greater than 2 are neglected, then a reduced order model which describes the behavior dominant harmonic results,

$$\frac{P_L(s)}{P_0(s)} = \frac{1}{\left(\frac{LV}{A_c c^2}\right)\left\{\left(\frac{LA_c}{2V}\right)\left[1+\frac{(LR_a)^2}{12(\bar{\rho}c)^2}\right]+\left[1+\frac{(LR_a)^2}{6(\bar{\rho}c)^2}\right]\right\}s^2+\left(\frac{L^2}{2c^2}+\frac{LV}{A_c c^2}\right)\frac{R_a}{\bar{\rho}}s+1} \tag{A-10}$$

For fully developed laminar flow conditions, the acoustical impedance is a constant. In addition, equation A-10 is a linear filter of the form

$$\frac{P_L(s)}{P_0(s)} = \frac{1}{\frac{1}{\omega_n^2}s^2+2\frac{\xi}{\omega_n}s+1} \tag{A-11}$$

with natural frequency, damping ratio, and time lag

$$\omega_n^{\,2} = \frac{\left(\frac{A_c c^2}{LV}\right)}{\left\{\left(\frac{LA_c}{2V}\right)\left[1+\frac{(LR_a)^2}{12(\bar{\rho}c)^2}\right]+\left[1+\frac{(LR_a)^2}{6(\bar{\rho}c)^2}\right]\right\}} \tag{A-12}$$

$$\xi = \frac{R_a\omega_n}{2\bar{\rho}}\left[\frac{L^2}{2c^2}+\frac{LV}{A_c c^2}\right] \tag{A-13}$$

$$\tau = \frac{2\xi}{\omega_n} = \frac{4R_aL\left[V+\frac{LA_c}{2}\right]}{\pi D^2 c^2\bar{\rho}} = \frac{128\mu}{c^2\bar{\rho}}\cdot\frac{L}{\pi D^2}\left[V+\frac{LA_c}{2}\right] \tag{A-14}$$

Development of Extrapolation Rules for Fully Developed Laminar Flow Conditions

Clearly, equation A-14 contains two groups of terms: those which depend on the geometry only and those which depend on properties of the local flow, such as $\bar{\rho}$, μ, and c^2. Because the geometry is fixed for a given measurement configuration, the time constant may be extrapolated to various flight conditions (assuming constant γ) according to the rule

$$\frac{\tau_f}{\tau_g} = \left[\frac{\mu}{c^2\bar{\rho}}\right]_f \times \left[\frac{\mu}{c^2\bar{\rho}}\right]_g^{-1} = \left[\frac{\mu}{\gamma R_g T\bar{\rho}}\right]_f \times \left[\frac{\gamma R_g T\bar{\rho}}{\mu}\right]_g = \left[\frac{\mu}{p}\right]_f \times \left[\frac{p}{\mu}\right]_g \tag{A-15}$$

Here again, the values for μ, $\bar{\rho}$, T, and p are the longitudinal averages. The expression for natural frequency (equation (A-12)) does not neatly decouple into flow and geometry terms;

$$\frac{[\omega_n]_f}{[\omega_n]_g} = \left[\frac{c}{\sqrt{\left\{\left(\frac{LA_c}{2V}\right)\left[1+\frac{(LR_a)^2}{12(\bar{\rho}c)^2}\right]+\left[1+\frac{(LR_a)^2}{6(\bar{\rho}c)^2}\right]\right\}}}\right]_f \times \left[\frac{\sqrt{\left\{\left(\frac{LA_c}{2V}\right)\left[1+\frac{(LR_a)^2}{12(\bar{\rho}c)^2}\right]+\left[1+\frac{(LR_a)^2}{6(\bar{\rho}c)^2}\right]\right\}}}{c}\right]_g \tag{A-16}$$

For laminar flow conditions, however, it can be shown with an order of magnitude analysis that

$$\frac{(LR_a)^2}{12(\bar{\rho}c)^2} < \frac{(LR_a)^2}{6(\bar{\rho}c)^2} \ll 1 \tag{A-17}$$

and the extrapolation rule reduces to the practical relationship

$$\frac{[\omega_n]_f}{[\omega_n]_g} \approx \frac{(c)_f}{(c)_g} = \sqrt{\frac{T_f}{T_g}} \tag{A-18}$$

The damping ratio is computed directly from the natural frequency and time lag. The second-order filter given by equation A-11 with parameters given by equations A-12 and A-13 will be used to perform the deconvolution analysis.

APPENDIX B

ESTIMATION OF SYSTEM PARAMETERS FROM STEP-RESPONSE DATA

The system parameters, ξ and ω_n, were extracted from the step-response data using a linearized least-squares technique. As discussed in appendix A, the system response is described as a second-order system whose frequency domain equation can be written as

$$P_L(s) = \frac{P_0(s)}{\left[\frac{1}{\omega_n^2}s^2 + 2\frac{\xi}{\omega_n}s + 1\right]} \tag{B-1}$$

Where P_L is the measured pressure, P_0 is the input pressure.

Transformation to Discrete Filter

If the second-order system model is discretized using the bi-linear transform (ref. 16),

$$s = \frac{2}{\Delta T}\frac{z-1}{z+1} \tag{B-2}$$

Where, ΔT is the sample interval of the system. Then when equation B-2 is substituted into equation B-1 and like powers in z are collected, the resulting discrete transfer function is

$$\left[\left(1 + \frac{4}{[\Delta T\omega_n]^2} + \frac{4\xi}{\Delta T\omega_n}\right)z^2 + \left(2 - \frac{8}{[\Delta T\omega_n]^2}\right)z + \left(1 + \frac{4}{[\Delta T\omega_n]^2} - \frac{4\xi}{\Delta T\omega_n}\right)\right]P_L(z) = \left[z^2 + 2z + 1\right]P_0(z) \tag{B-3}$$

Letting

$$A[0] = 1 + \frac{4}{[\Delta T\omega_n]^2} - \frac{4\xi}{\Delta T\omega_n} \tag{B-4}$$

$$A[1] = 2 - \frac{8}{[\Delta T\omega_n]^2} \tag{B-5}$$

$$A[2] = 1 + \frac{4}{[\Delta T\omega_n]^2} + \frac{4\xi}{\Delta T\omega_n} \tag{B-6}$$

B-3 reduces to

$$\left[A[2]z^2 + A[1]z + A[0]\right]P_L(z) = \left[z^2 + 2z + 1\right]P_0(z) \tag{B-7}$$

Transforming to the time domain using the transformation rule yields (ref. 16)

$$z^n[x(z)] = x_{k+n} \tag{B-8}$$

The resulting difference equation is

$$A[2]P_{L_{k+2}} + A[1]P_{L_{k+1}} + A[0]P_{L_k} = P_{0_{k+2}} + 2P_{0_{k+1}} + P_{0_k} \tag{B-9}$$

with k as the time index.

Formulation of Matrix Equations and Least-Squares Solution

If $N+1$ data points are available, then equation B-9 may be written as the over-determined system of linear equations. For example,

$$\begin{bmatrix} P_{L_2} & P_{L_1} & P_{L_0} \\ P_{L_3} & P_{L_2} & P_{L_1} \\ P_{L_4} & P_{L_3} & P_{L_2} \\ \cdots & \cdots & \cdots \\ \cdots & \cdots & \cdots \\ P_{L_{N-2}} & P_{L_{N-3}} & P_{L_{N-4}} \\ P_{L_{N-1}} & P_{L_{N-2}} & P_{L_{N-3}} \\ P_{L_N} & P_{L_{N-1}} & P_{L_{N-2}} \end{bmatrix} \begin{bmatrix} A[2] \\ A[1] \\ A[0] \end{bmatrix} = \begin{bmatrix} P_{0_2} + 2P_{0_1} + P_{0_0} \\ P_{0_3} + 2P_{0_2} + P_{0_1} \\ P_{0_4} + 2P_{0_3} + P_{0_2} \\ \cdots \\ \cdots \\ P_{0_{N-2}} + 2P_{0_{N-3}} + P_{0_{N-4}} \\ P_{0_{N-1}} + 2P_{0_{N-2}} + P_{0_{N-3}} \\ P_{0_N} + 2P_{0_{N-1}} + P_{0_{N-2}} \end{bmatrix} \tag{B-10}$$

Using the pseudoinverse method (ref. 18), which is equivalent to performing linear least-squares estimation, to solve equation B-10 for the difference equation coefficients, $A[0]$, $A[1]$, $A[2]$, then the natural frequency and damping ratio can be computed by manipulation of the original relationships

$$\omega_n = \frac{4}{\Delta T\sqrt{A[0] + A[2] - A[1]}} \tag{B-11}$$

$$\xi = \frac{A[2] - A[0]}{2\sqrt{A[0] + A[2] - A[1]}} \tag{B-12}$$

APPENDIX C

DEVELOPMENT OF OPTIMAL DECONVOLUTION ALGORITHM

In this appendix, the algorithm for reconstructing the "true" input pressure from the raw data is developed. This algorithm is based on the methods of spectral convolution, and the resulting algorithm is implemented as a frequency domain filter. Conceptually, it is a trivial matter to compensate for the effects of the acoustical distortion by taking the numerical Fourier transform of the raw pressure data, multiplying by the inverse of the transfer function, and taking the numerical inverse transform. This method is referred to as *spectral deconvolution*. In practice, however, the implementation is not easy.

Clearly, the measurement system will have some nominal signal-to-noise ratio, Rs_n, which represents the fundamental accuracy of the measurement system. The noise is introduced into the measured signal by the transducer, its associated electronics, and the quantization of the measurement system. The measurement noise is typically white over the range of the sampled spectrum; however, this noise may contain concentrated regions of spectral energy, such as noise introduced by electromagnetic interference.

Regardless of the noise characteristics of the system, for pneumatic data at higher frequencies, the measured signal is attenuated. In addition, the signal-to-noise ratio drops considerably below the nominal value. At high frequencies where the measured signal is attenuated, the deconvolution transfer function acts as an amplifier. This function will amplify the attenuated signal and the additive measurement noise. This overamplification produces a very noisy reconstructed signal. Thus, an inversion filter which controls and minimizes noise amplification must be developed.

Development of Compensation Filter

Assuming that the dynamics of the pneumatic distortion are described by the second-order model developed in appendix A,

$$\frac{d^2 p_L(t)}{dt^2} + 2\xi\omega_n \frac{dp_L(t)}{dt} + \omega_n^2\, p_L(t) = \omega_n^2 p_0(t) \tag{C-1}$$

where p_L is the measured pressure value, and p_0 is the input surface pressure. Then, the noisy pressure measurements can be modeled by the convolution

$$p_L(t) = \int_0^t \upsilon(t-\tau_c) p_0(\tau_c) d\tau_c + \eta(t) \tag{C-2}$$

where $\upsilon(t-\tau)$ is the convolution function, and $\eta(t)$ is additive measurement noise. For this analysis, it is assumed that the measurement noise is unbiased. That is, $E[\eta(t)] = 0$. Because the noise is introduced by the measurement system, it is uncorrelated with the surface pressure. For example, $E[p_0(t)\eta(t)] = 0$.

The Fourier transform of equation C-2 is

$$P_L(\omega) = \Upsilon(\omega) P_0(\omega) + H(\omega) \tag{C-3}$$

where $P_L(\omega)$, $P_0(\omega)$, and $H(\omega)$ are the Fourier transforms of the measurement, input, and noise function time series, and ω is the radian frequency parameter. Because the noise in unbiased,

$$E[H(\omega)] = E\{F[\eta(t)]\} = \int_{-\infty}^{\infty} e^{-j\omega t} E[\eta(t)]dt = 0 \tag{C-4}$$

Similarly, because the input pressure and measurement noise are uncorrelated,

$$E[P_0(\omega)H(\omega)] = E\left\{\int_{-\infty}^{\infty} e^{-j\omega\tau_c} p_L(\tau_c)d\tau_c \int_{-\infty}^{\infty} e^{-j\omega t}\eta(t)dt\right\} \tag{C-5}$$

$$= E\left\{\int_{-\infty}^{\infty} e^{-j\omega\tau_c}\left[\int_{-\infty}^{\infty} e^{-j\omega t}[p_L(\tau_c)\eta(t)]dt\right]d\tau_c\right\}$$

$$= \int_{-\infty}^{\infty} e^{-j\omega\tau_c}\left[\int_{-\infty}^{\infty} e^{-j\omega t} E[p_L(\tau_c)\eta(t)]dt\right]d\tau_c = 0$$

The goal is to select an inversion filter, $G(\omega)$, such that the surface pressure estimate minimizes the squared difference between the estimated surface pressure and the actual value; that is, seek an optimal filter of the form

$$\hat{P}_0(\omega) = G(\omega)P_L(\omega) \tag{C-6}$$

which minimizes the cost functional

$$J(\omega) = E\left[(\hat{P}_0(\omega) - P_0(\omega))^* (\hat{P}_0(\omega) - P_0(\omega))\right] \tag{C-7}$$

subject to the constraints of equation C-1. The optimization method used to develop this filtering algorithm was first developed by Norbert Weiner. The resulting filter can correctly be referred to as a *Weiner Filter* (ref. 19).

Substituting for $\hat{P}_0$ in equation C-7

$$J(\omega) = E\left[\left(G(\omega)P_L(\omega) - P_0(\omega)\right)^* \left(G(\omega)P_L(\omega) - P_0(\omega)\right)\right] \tag{C-8}$$

Dropping the (ω) notation and expanding terms in equation C-8, the cost functional becomes

$$J = E\left[G^* G P_L^* P_L - P_0^* G P_L - G^* P_L^* P_0 + P_0^* P_0\right] \tag{C-9}$$

$$= G^* G E\left[P_L^* P_L\right] - G E\left[P_0^* P_L\right] - G^* E\left[P_L^* P_0\right] + E\left[P_0^* P_0\right]$$

This notation is assumed implicit for simplicity of notation. Defining

$$A_{LL} = E\left[P_L^* P_L\right]$$

$$A_{LO} = E\left[P_L^* P_0\right]$$

$$A_{OL} = E\left[P_0^* P_L\right] = A_{LO}^*$$

$$A_{OO} = E\left[P_0^* P_0\right]$$

Then,

$$J = G^* G A_{LL} - G A_{LO}^* - G^* A_{LO} + A_{OO} \tag{C-10}$$

Letting $\text{Real}(G) = G_r$, $\text{Im}(G) = G_{im}$, $\text{Real}(A_{LO}) = A_{LO_r}$, $\text{Im}(A_{LO}) = A_{LO_{im}}$; then, $G \equiv G_r + jG_{im}$, $A_{LO} \equiv A_{LO_r} + jA_{LO_{im}}$. In addition, and substitution into equation C-10 gives

$$\begin{aligned} J &= (G_r - jG_{im})(G_r + jG_{im})A_{LL} - (G_r + jG_{im})(A_{LO_r} - jA_{LO_{im}}) - (G_r - jG_{im})(A_{LO_r} + jA_{LO_{im}}) + A_{OO} \\ &= (G_r^2 + G_{im}^2)A_{LL} - 2(G_r A_{LO_r} + G_{im} A_{LO_{im}}) + A_{OO} \end{aligned} \tag{C-11}$$

Because values for A_{LO}, A_{LL}, and A_{OO} are defined by the expectation values for the measured and true input pressures (defined above), G_r and G_{im} are the only free parameters of the system, and necessary and sufficient conditions for optimization (ref. 15) of the cost index are (holding frequency constant)

$$\frac{\partial J}{\partial G_r} = 0, \quad \frac{\partial J}{\partial G_{im}} = 0 \tag{C-12}$$

Computing the partial derivatives yields

$$\frac{\partial J}{\partial G_r} = 2\hat{G}_r A_{LL} - 2[A_{LO_r}] = 0, \quad \Rightarrow \hat{G}_r = \frac{A_{LO_r}}{A_{LL}}$$

$$\Rightarrow \hat{G} = \hat{G}_r + j\hat{G}_{im} = \frac{A_{LO_r} + jA_{LO_{im}}}{A_{LL}} = \frac{A_{LO}}{A_{LL}} = \frac{E[P_L^* P_0]}{E[P_L^* P_L]}$$

$$\frac{\partial J}{\partial G_{im}} = 2\hat{G}_{im} A_{LL} - 2[A_{LO_{im}}] = 0, \quad \Rightarrow \hat{G}_{im} = \frac{A_{LO_{im}}}{A_{LL}} \tag{C-13}$$

The optimal estimate of the input pressure spectrum based on the measured pressure spectrum and the constraints of the dynamics model is

$$\hat{P}_0(\omega) = \left[\frac{E\left[P_L^* P_0\right]}{E\left[P_L^* P_L\right]}\right] P_L(\omega) \tag{C-14}$$

The numerator of equation C-14 depends on the correlation of the measured pressure to the true input pressure, an unknown value. Using the measurement model, equation C-6, however, equation C-14 can be written in terms of the expected values for the input pressure and the measurement noise.

$$\hat{P}_0(\omega) = \left[\frac{E[P_L^*\, P_0]}{E[P_L^*\, P_L]}\right] P_L(\omega) = \left[\frac{E[(\Upsilon^*\, P_0^* + H^*) P_0]}{E[(\Upsilon^*\, P_0^* + H^*)(\Upsilon P_0 + H)]}\right] P_L(\omega) \tag{C-15}$$

$$= \left[\frac{\Upsilon^*\, E[P_0^*\, P_0] + E[H^*\, P_0]}{\Upsilon^*\, \Upsilon\, E[P_0^*\, P_0] + \Upsilon\, E[H^*\, P_0] + \Upsilon^*\, E[P_0^*\, H] + E[H^*\, H]}\right] P_L(\omega)$$

Because $E[P_0^*(\omega) H(\omega)] = 0$, then

$$\hat{P}_0(\omega) = \left[\frac{\Upsilon^*\, E[P_0^*\, P_0]}{\Upsilon^*\, \Upsilon\, E[P_0^*\, P_0] + E[H^*\, H]}\right] P_L(\omega) \tag{C-16}$$

Defining $\|P_0\|_\omega^2 = E[P_0^*(\omega) P_0(\omega)]$, $\|H\|_\omega^2 = E[H^*(\omega) H(\omega)]$, the optimal deconvolution algorithm becomes

$$\hat{P}_0(\omega) = \left[\frac{\Upsilon^* \|P_0\|_\omega^2}{\Upsilon^*\, \Upsilon \|P_0\|_\omega^2 + \|H\|_\omega^2}\right] P_L(\omega) = \left[\frac{\Upsilon^*(\omega) \dfrac{\|P_0\|_\omega^2}{\|H\|_\omega^2}}{|\Upsilon(\omega)|^2 \dfrac{\|P_0\|_\omega^2}{\|H\|_\omega^2} + 1}\right] P_L(\omega) \tag{C-17}$$

Equation C-17 weights the Fourier coefficients of the deconvolution as a function of the measured signal-to-noise power spectrum ratio,

$$\frac{\|P_0(\omega)\|^2}{\|H(\omega)\|^2} \tag{C-18}$$

which is closely approximated by the nominal signal-to-noise ratio of the system. Clearly, as the signal-to-noise ratio increases, the optimal deconvolution algorithm becomes a simple deconvolution.

$$\hat{P}_0(\omega) \Rightarrow \left[\frac{1}{\Upsilon^*}\right] P_L(\omega) \tag{C-19}$$

Equation C-17 is the final form of the optimal deconvolution algorithm.

Evaluation of Signal-to-Noise Ratio for the SR-71 Sonic Boom Tests

For the sonic boom analysis, the measurement noise was assumed to be white. Based on the manufacturer's accuracy specifications of ± 0.0075 percent of full-scale, and a full-scale value of 2736 psf (19 psi), the nominal signal-to-noise ratio of the measurement system is

$$Rs_n \approx \frac{\|P_L(t)\|^2}{\left[0.000075 \times P_{\text{full scale}}\right]^2} \approx \frac{\Psi^2_{P_L}}{\left[0.21_{\text{psf}}\right]^2} \tag{C-20}$$

Here, $\Psi^2_{P_L}$, is the mean square of the measured time history over the course of the maneuver.

Effects of Time Series Truncation

For practical implementation using the fast Fourier transform (FFT), great care must be taken to avoid finite-sized windowing effects (ref. 19). Such effects would be amplified by the deconvolution algorithm. Truncation of a time series at $t \pm t_c$ is equivalent to multiplying by a "truncation boxcar." The "resolution bandwidth," the smallest frequency which can be independently resolved by the finite length Fourier transform, is inversely proportional to the length of the time window. When power is distributed at frequencies which are separated by less than the resolution, these bandwidths are smeared together. For this analysis the effects of truncation smearing can be mitigated by using a "taper window" before the transform of the original time series. Window selection has been researched extensively (ref. 19). Generally, the focus has been on choosing a truncation function so that the effects induced by the frequency domain convolution are reduced. For this analysis, a "cosine taper" window is used to mitigate these effects. This window is defined as

$$T_{\cos}(t) = \left\{ \begin{array}{ll} \frac{1}{2}\left\{1 - \cos\left(\pi\kappa\left[1 - \frac{t}{t_c}\right]\right)\right\} & \text{for} \quad |t| > \left|\left(1 - \frac{1}{\kappa}\right)t_c\right| \\ 1 & \text{for} \quad |t| < \left|\left(1 - \frac{1}{\kappa}\right)t_c\right| \end{array} \right\} \tag{C-21}$$

Here, κ is a parameter which gives a degree of freedom to the window, and it is selected by engineering judgment. For the sonic boom analysis, a value of $\kappa = 5$ was sufficient.

Implementation of the Inverse Transform

To ensure that a real-time series results when the frequency spectrum is inversely transformed, the discrete spectrum should be skewed symmetric about the Nyquist frequency. For the discrete series, the upper half of the spectrum should obey the relationship

$$\hat{P}_0\left(\omega\left[\frac{N}{2} + 1 + i\right]\right) = \left\{\hat{P}_0\left(\omega\left[\frac{N}{2} + 1 - i\right]\right)\right\}^* \quad i = 1, \frac{N}{2} - 1 \tag{C-22}$$

As with the forward Fourier transform, the inverse transform also has windowing effects. The inverse transform is approximated by a finite sum. The truncated harmonics, which are a "window" in the frequency domain, induce a convolution in the time domain. This convolution causes unwanted oscillations in the resulting time series, a process known as Gibb's phenomenon (ref. 19). To eliminate these oscillations, the deconvolved time series is filtered by taking weighted averages of adjacent time points, such as

$$\beta_k = \sum_{i=-\lambda}^{\lambda} g_i p_{i+k} \tag{C-23}$$

The parameter, λ, is a degree of freedom that must be selected using engineering judgment. The filter weights are arbitrary as long as they satisfy the relationship

$$\sum_{i=-\lambda}^{\lambda} g_i = 1 \tag{C-24}$$

to prevent a change in the direct current (dc) level of the signal. For this analysis, a window length of 9 ($\lambda = 4$) was sufficient. For the sonic boom tests, constant weights of magnitude $g_i = \left\{\frac{1}{25}, \frac{2}{25}, \frac{3}{25}, \frac{4}{25}, \frac{1}{5}, \frac{4}{25}, \frac{3}{25}, \frac{2}{25}, \frac{1}{25}\right\}$ were sufficient.

Collected Algorithm

Figure C-1 shows the collected deconvolution algorithm. Here, the time series is windowed using equation C-9 to reduce truncation smearing. Next, the transform is performed, and the spectra are deconvolved using the algorithm of equation C-17. The upper half of the spectrum is created using equation C-22, and the inverse transform is performed. Any Gibb's ringing in the resulting time series is eliminated using the simple filter of equation C-23. Finally, any effects caused by the original taper window are masked off of the deconvolved time history.

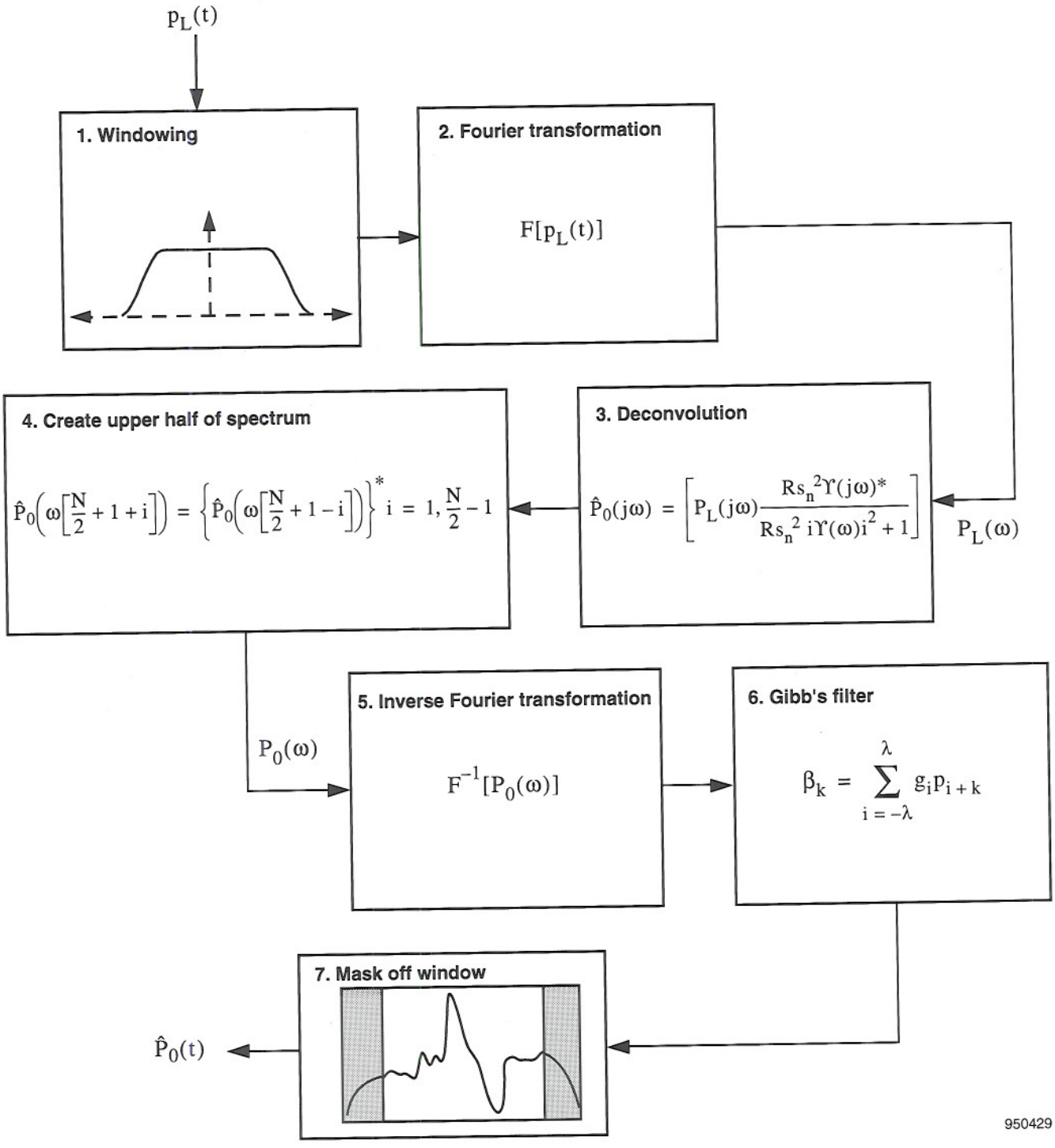

Figure C-1. Spectral deconvolution scheme.

APPENDIX D

SIMULATION OF TUBE DYNAMICS FOR A STEP INPUT

To determine the linear response region of the F-16XL airdata system, it became necessary to compute the longitudinally and radially averaged Reynolds number in the noseboom tubing as a function of step input size. This appendix describes the computational scheme used to perform the analysis. The analysis examines a small slice of pressure tubing where the flow is assumed to be axisymmetric. Flow perturbations are small. In addition, flow is parallel to the tubing walls. For axisymmetric channel flow, the Navier-Stokes equations momentum equation (ref. 16) may be written as

$$\bar{\rho}\frac{\partial[u(r,x,t)]}{\partial t}+\frac{\partial[p(x,t)]}{\partial x}=\mu\frac{1}{r}\left(\frac{\partial}{\partial r}\left[r\frac{\partial u(r,x,t)}{\partial r}\right]\right) \tag{D-1}$$

where $u(r, x, t)$ is the flow velocity in the tube, r is the radial distance from the axis of symmetry, μ is the dynamic viscosity, and $\bar{\rho}$ is the mean flow density. The longitudinal shearing stress is given by

$$\tau_s(r)=-\mu\frac{\partial u}{\partial r} \tag{D-2}$$

and

$$\bar{\rho}\frac{\partial[u(r,x,t)]}{\partial t}+\frac{\partial[p(x,t)]}{\partial x}=\frac{1}{r}\left(\frac{\partial}{\partial r}\left[r\,\mu\frac{\partial u(r,x,t)}{\partial r}\right]\right)=-\frac{1}{r}\left(\frac{\partial}{\partial r}[r\,\tau_s(r)]\right) \tag{D-3}$$

Taking the radial average of equation D-3

$$\frac{1}{\pi R^2}\int_0^{2\pi}\int_0^R\frac{1}{r}\left(\frac{\partial}{\partial r}[r\,\tau_s(r)]\right)r\;dr\;d\theta=\frac{2\pi}{\pi R^2}\left|r\tau_s(r)\right|_O^R=\frac{2\tau_{sw}}{R} \tag{D-4}$$

where τ_{sw} is the wall-shearing stress, and R is the tube radius at station x. Defining

$$\tau_{sw}=C_f\frac{\bar{\rho}U^2}{2} \tag{D-5}$$

then

$$\frac{2\tau_{sw}}{R}=\frac{2C_f}{R}\frac{\bar{\rho}U^2}{2}=\frac{2C_f}{D}\bar{\rho}U^2\frac{D}{\mu}\frac{\mu}{D}=\frac{2\mu C_f}{D^2}\frac{\bar{\rho}UD}{\mu}U=\frac{2\mu C_f}{D^2}R_{ey}\,U \tag{D-6}$$

In addition, the radial average of equation D-1 is written as

$$\frac{\partial[U(x,t)]}{\partial t}+\frac{2\mu C_f}{D^2}\frac{R_{ey}}{\bar{\rho}}U(x,t)+\frac{1}{\bar{\rho}}\frac{\partial[p(x,t)]}{\partial x}=0 \tag{D-7}$$

where, $U(x,t)$ is the radial average of the velocity at station x and time t. Recalling from appendix A that the acoustical impedance, R_a, is defined as

$$R_a = \frac{2\mu R_{ey} C_f}{D^2} \tag{A-3}$$

then

$$\frac{\partial[U(x,t)]}{\partial t} + \frac{R_a}{\bar{\rho}} U(x,t) + \frac{1}{\bar{\rho}} \frac{\partial[p(x,t)]}{\partial x} = 0 \tag{D-8}$$

Across a section of tubing of length, L, if equation D-8 is integrated with respect to x,

$$\int_0^L \left[\frac{\partial[U(x,t)]}{\partial t} + \frac{R_a}{\bar{\rho}} U(x,t)\right] dx = \frac{\partial}{\partial t}\int_0^L U(x,t)dx + \int_0^L \left[\frac{R_a}{\bar{\rho}} U(x,t)\right] dx = \frac{1}{\bar{\rho}}[p(0,t) - p(L,t)] \tag{D-9}$$

Defining

$$\frac{1}{L}\int_0^L U(x,t)dx = \bar{U}(t) \tag{D-10}$$

the expression for the average velocity as a function of the pressure difference across the tubing section results

$$\frac{\partial}{\partial t} \bar{U}(t) + \frac{R_a}{\bar{\rho}} \bar{U}(t) = \frac{1}{\bar{\rho}} \frac{[\, p(0,t) - p(L,t)]}{L} \tag{D-11}$$

Recall from appendix A that for laminar conditions

$$C_f = \frac{16}{R_{ey}}; \text{ thus, } R_a = \frac{32\mu}{D^2} \tag{A-4) and (A-5}$$

and for turbulent conditions reference 15 gives

$$C_f = \frac{\tau_{sw}}{\frac{1}{2}\bar{\rho}U^2} = \frac{1}{4}\left(\frac{0.3164}{R_{ey}^{1/4}}\right); \text{ thus, } R_a = \frac{0.1582\mu[R_{ey}]^{3/4}}{D^2} \tag{D-12) and (D-13}$$

Because the average Reynolds number is a function of $\bar{U}(t)$, in the general case, equation D-11 is nonlinear and must be numerically solved to simulate the flow as a function of time. A predictor-corrector method is used to solve equation D-11. The equation is first discretized at a time interval ΔT using explicit time differences and is used to predict the response based on the pressure differential and the acoustical impedance at the previous time frame

$$U_{k+1} = \left[1 - \frac{\Delta T R_{a_k}}{\bar{\rho}}\right] \bar{U}_k + \frac{\Delta T}{\bar{\rho}} \frac{\left[p_0 - P_L\right]_k}{L} \tag{D-14}$$

The Reynolds number and acoustical impedance are then re-evaluated using the predicted velocity.

$$\tilde{R}_{ey_{k+1}} = \frac{\bar{\rho} U_{k+1} D}{\mu} \tag{D-15}$$

and

$$\tilde{R}_{a_{k+1}} = \frac{2\mu \tilde{R}_{ey_{k+1}} C_f}{D^2} \tag{D-16}$$

where (ref. 15)

$$C_f = \frac{16}{\tilde{R}_{ey}} \text{ for } \tilde{R}_{ey} < 2300 \tag{D-17}$$

$$C_f = \frac{0.0791}{[\tilde{R}_{ey}]^{1/4}} \text{ for } \tilde{R}_{ey} > 4000 \tag{D-18}$$

For $2300 < \tilde{R}_{ey} < 4000$, a linear interpolation of the friction coefficients was used. The result of equation D-14 is corrected using the new value for the acoustical impedance from equation D-16 and the pressure differential from the current data frame.

$$U_{k+1} = \frac{U_k + \frac{\Delta T}{\bar{\rho}} \frac{[p_0 - p_L]_{k+1}}{L}}{\left[1 + \frac{\Delta T \tilde{R}_{a_{k+1}}}{\bar{\rho}}\right]} \tag{D-19}$$

After equation D-19, the Reynolds number and acoustical impedance values were updated using the new velocity. Then, the cycle was repeated for the next data frame. The algorithm defined by equations D-14 and D-19 will remain stable as long as

$$\Delta T < \frac{2\bar{\rho}}{\tilde{R}_{a_k}} \tag{D-20}$$

For this analysis, the length of the tubing, L, was assumed to be length of the tubing from the input port to the digital pressure transducer. The effects of branches downstream of the digital transducer were ignored. Based on these lengths for the static and total pressure systems, the effective diameters and volumes were evaluated by iteratively solving equations D-14, D-15, and B-1 using the experimental data from table 2 to evaluate the time constants and natural frequencies. The equations were solved in an ad-hoc manner until a consistent match of the system parameters resulted. The resulting geometry parameters are summarized in table D-1.

Table D-1. Parameters used for simulation of tube dynamics.

Pressure	ξ	ω_n, rad/sec	V_{eff}, in^3	L, in.	D_{eff}, in.
Total	0.841	17.47	6.8	140	0.114
Static	2.254	8.485	24	140	0.100

APPENDIX E

NOMENCLATURE

ANS	astro-navigation system
CAD	central airdata
dc	direct current
FFT	fast Fourier transform
INS	inertial navigation system
PCM	pulse code modulation

Symbols

$A[0], A[1], A[2]$	difference equation coefficients
A_c	tube cross-section area
A_{LL}	expectation operator coefficient at $x = L$
A_{LO}	expectation operator coefficient for $x = L$ to 0
A_{OL}	expectation operator coefficient for $x = 0$ to L
A_{OO}	expectation operator coefficient at $x = 0$
c	sonic velocity
C_f	skin friction coefficient
D	tube diameter
E	expectation operator
F	Fourier transform operator
g	Gibb's weighting constants
G	optimal filter function
j	$\sqrt{-1}$
J	cost function
k	time index
L	tube length
m	summation index
M_∞	freestream Mach number
n	data point index
N	number of data points
p	pressure, time domain
P	pressure, frequency domain
r	radial distance

R	tube radius
R_a	acoustic impedance
R_{ey}	Reynolds number
R_g	ideal gas constant
Rs_n	signal-to-noise ratio
s	frequency domain variable
t	time
t_c	truncation time limit
T	temperature
$T_{\cos}$	cosine taper truncation window
$u(r, x, t)$	tube velocity
$U(x, t)$	radial average of tube velocity
V	volume
x	longitudinal distance
z	Z-transform variable
α	square of damped radian frequency
β	weighted averages
γ	ratio of specific heats for air
δp	overpressure, psi, psf
ΔT	sample interval
η	measurement noise function, time domain
H	measurement noise function, frequency domain
θ	tube azimuth
κ	truncation window degree of freedom
λ	weighted averages degree of freedom
μ	dynamic viscosity
ξ	damping ratio
$\bar{\rho}$	longitudinal average of tubing density
σ	standard deviation
τ	time lag
τ_c	convolution parameter
τ_s	longitudinal shearing stress
τ_{sw}	wall-shearing stress
υ	convolution function, time domain
Υ	convolution function, frequency domain
$\Psi^2_{P_L}$	mean square of measured pressure, psf^2

ω	frequency
ω_n	natural frequency

Subscripts and Superscripts

$\hat{}$	estimated parameter
$*$	conjugate of complex number or function
$\tilde{}$	predicted step
$\bar{}$	longitudinal average
eff	effective
f	parameter evaluated for flight conditions
g	parameter evaluated for ground test conditions
i	index number
im	imaginary part of complex number
L	at end of tube of length *L* (measured)
r	real part of complex number
0	at beginning of tube (input)

REFERENCES

[1] Whitman, G.B., "The Flow Pattern of a Supersonic Projectile," *Communications on Pure and Applied Mathematics*, vol. V, no. 3, Aug. 1952, pp. 301–348.

[2] Stephens, R.W.B. and Bate, A.E., *Acoustics and Vibrational Physics*, St. Martin Press, New York, 1966.

[3] National Research Council, Aeronautical Technologies for the Twenty-First Century, National Academy Press, Washington, D.C., 1992.

[4] Edward A. Haering, Jr., Stephen A. Whitmore, and L.J. Ehernberger, "Measurement of the Basic SR-71 Airplane Near-Field Signature," NASA CDCP-1001, 1994. Also presented at NASA High Speed Research Program Sonic Boom Workshop, NASA Langley Research Center, Hampton, VA 23681-0001, June 1–3, 1994. L-17435, pp. 171–197.

[5] Mullens, Marshall E., *A Flight Test Investigation of the Sonic Boom*, AFFTC TN-56-20, May 1956.

[6] Smith, Harriet J., *Experimental and Calculated Flow Fields Produced by Airplanes Flying at Supersonic Speeds*, NASA TN D-621, 1960.

[7] Maglieri, Domenic J., Ritchie, Virgil S., and Bryant, John F., Jr., *In-Flight Shock-Wave Pressure Measurements Above and Below a Bomber Airplane at Mach Numbers from 1.42 to 1.69*, NASA TN D-1968, 1963.

[8] Urie, D., *Lockheed SR-71 Researcher's Handbook*, Lockheed Advanced Development Company, Sunland, California, 1990. (Available from National Academy Press, 2101 Constitution Ave. N.W., Washington, D.C.)

[9] McGlamry, A., *F-16 XL Phase I, Follow On Performance Testing: Final Report*, AFFTC-TR-84-16, Aug. 1984.

[10] Haering, Edward A., Jr., and Whitmore, Stephen A., *FORTRAN Program for Analyzing Ground-Based Radar Data: Usage and Derivations, Version 6.2*, NASA TP-3430, 1995.

[11] Ehernberger, L.J., Haering, Edward A., Jr., Lockhart, Mary G., and Teets, Edward H., "Atmospheric Analysis for Airdata Calibration on Research Aircraft," AIAA 92-0293, Jan. 1992.

[12] National Oceanic and Atmospheric Administration, *United States Standard Atmosphere*, 1976, NOAA S/T 76-1562, Oct. 1976.

[13] Liepmann, H.W. and Roshko, A., *Elements of Gas Dynamics*, 3rd ed, Wiley & Sons, New York, 1956.

[14] Whitmore, Stephen A. and Moes, Timothy R., *The Effects of Pressure Sensor Acoustics on Airdata Derived from a High-Angle-of-Attack Flush Airdata Sensing (HI-FADS) System*, NASA TM-101736, 1991.

[15] Freiberger, W.F., ed., *The International Dictionary of Applied Mathematics*, Nostrand Co., Princeton, 1960.

[16] Schlicting, Hermann, *Boundary Layer Theory*, 7th ed., trans. J. Kestin, New York, 1979.

[17] Franklin, G.F. and Powell, J.D., *Digital Control of Dynamic Systems*, Addison Wesley, Reading, 1980.

[18] Golub, Gene H. and Van Loan, Charles F., *Matrix Computations*, Johns Hopkins UP, Baltimore, 1983, pp. 86–90.

[19] Bendat, Julius S. and Piersol, Allan G., *Random Data: Analysis and Measurement Procedures*, Wiley & Sons, New York, 1971.

REPORT DOCUMENTATION PAGE

Form Approved
OMB No. 0704-0188

1. AGENCY USE ONLY (Leave blank)	2. REPORT DATE	3. REPORT TYPE AND DATES COVERED
	June 1996	~~Controlled Distribution~~ Technical Paper

4. TITLE AND SUBTITLE

An Optimal Deconvolution Method for Reconstructing Pneumatically Distorted Near-Field Sonic Boom Pressure Measurement

5. FUNDING NUMBERS

WU 505-37-03

6. AUTHOR(S)

Stephen A. Whitmore, Edward A. Haering, Jr., and L.J. Ehernberger

7. PERFORMING ORGANIZATION NAME(S) AND ADDRESS(ES)

NASA Dryden Flight Research Center
P.O. Box 273
Edwards, California 93523-0273

8. PERFORMING ORGANIZATION REPORT NUMBER

H-2054 ; H-2943

9. SPONSORING/MONOTORING AGENCY NAME(S) AND ADDRESS(ES)

National Aeronautics and Space Administration
Washington, DC 20546-0001

10. SPONSORING/MONITORING AGENCY REPORT NUMBER

NASA ~~CD~~TP-4000

11. SUPPLEMENTARY NOTES

All copies of this document or portions thereof shall include the cover with the restriction notice clearly displayed.

12a. DISTRIBUTION/AVAILABILITY STATEMENT

~~Available only with approval of High-Speed Research Program Intellectual Property Manager~~
~~NASA Dryden Flight Research Center, Edwards, California 93523-0273~~
Subject Category 05

12b. DISTRIBUTION CODE

Restriction changed to publicly available on March 13, 2009 by authority of the Aeronautics Mission Directorate.

13. ABSTRACT (Maximum 200 words)

In-flight measurements of the SR-71 near-field sonic boom were obtained by an F-16XL airplane at flightpath separation distances from 40 to 740 ft. Twenty-two signatures were obtained from Mach 1.60 to Mach 1.84 and altitudes from 47,600 to 49,150 ft. The shock wave signatures were measured by the total and static sensors on the F-16XL noseboom. These near-field signature measurements were distorted by pneumatic attenuation in the pitot-static system. The near-field pressure signatures were corrected by modeling the magnitude and phase of the pitot-static sensors and accounting for their effects using optimal deconvolution. Measurement system magnitude and phase characteristics were determined from ground-based step-response tests and extrapolated to flight conditions using analytical models. Deconvolution was implemented using Fourier transform methods. Comparisons of the shock wave signatures reconstructed from the total and static pressure data are presented. The good agreement achieved gives confidence of the quality of the reconstruction analysis. Although originally developed to reconstruct the sonic boom signatures from SR-71 sonic boom flight tests, the methods presented here generally apply to other types of highly attenuated or distorted pneumatic measurements.

14. SUBJECT TERMS

Airdata; Deconvolution; Flight test; F-16XL aircraft; Pressure sensing; Shock wave signatures; Sonic boom; SR-71 aircraft

15. NUMBER OF PAGES

37

16. PRICE CODE

AO3

17. SECURITY CLASSIFICATION OF REPORT	18. SECURITY CLASSIFICATION OF THIS PAGE	19. SECURITY CLASSIFICATION OF ABSTRACT	20. LIMITATION OF ABSTRACT
Unclassified	Unclassified	Unclassified	~~Limited~~ Unlimited